

Witnessing Quantum Entanglement Using Resonant Inelastic X-ray Scattering

Tianhao Ren,^{1,*} Yao Shen,^{1,2,3,†} Sophia F. R. TenHuisen,⁴ Jennifer Sears,¹ Wei He,¹ Mary H. Upton,⁵ Diego Casa,⁵ Petra Becker,⁶ Matteo Mitrano,⁴ Mark P. M. Dean,^{1,‡} and Robert M. Konik^{1,§}

¹*Condensed Matter Physics and Materials Science Division,
Brookhaven National Laboratory, Upton, New York 11973, USA*

²*Beijing National Laboratory for Condensed Matter Physics,
Institute of Physics, Chinese Academy of Sciences, Beijing 100190, China*

³*School of Physical Sciences, University of Chinese Academy of Sciences, Beijing 100049, China*

⁴*Department of Physics, Harvard University, Cambridge, Massachusetts 02138, USA*

⁵*Advanced Photon Source, Argonne National Laboratory, Argonne, Illinois 60439, USA*

⁶*Section Crystallography, Institute of Geology and Mineralogy, University of Cologne, 50939 Köln, Germany*
(Dated: April 10, 2024)

Although entanglement is both a central ingredient in our understanding of quantum many-body systems and an essential resource for quantum technologies, we only have a limited ability to quantify entanglement in real quantum materials. Thus far, entanglement metrology in quantum materials has been limited to measurements involving Hermitian operators, such as the detection of spin entanglement using inelastic neutron scattering. Here, we devise a method to extract the quantum Fisher information (QFI) from non-Hermitian operators and formulate an entanglement witness for resonant inelastic x-ray scattering (RIXS). Our approach is then applied to the model iridate dimer system $\text{Ba}_3\text{CeIr}_2\text{O}_9$ and used to directly test for entanglement of the electronic orbitals between neighboring Ir sites. We find that entanglement is challenging to detect under standard conditions, but that it could be achieved by analyzing the outgoing x-ray polarization or via specific choices of momentum and energy. Our protocol provides a new handle for entanglement detection, which offers routes to related types of entanglement witness (such as orbitally-resolved measurements) and to the generalization to out-of-equilibrium settings accessed in ultrafast settings.

INTRODUCTION

Multipartite quantum entanglement refers to the entanglement of a quantum system across multiples of its subsystems. While all entanglement measures express in some form the non-locality that is a fundamental aspect of quantum mechanics, the phenomenology of multipartite entanglement is, in general, much richer than that given by bipartite measures such as the Rényi and von Neumann entanglement entropies. Multipartite entanglement is also a driver of quantum technologies where entanglement across multiple sites acts as a resource [1] that enables quantum communication [2], enhanced quantum metrology [3], quantum sensing [4], quantum machine learning [5], and quantum imaging [6, 7]. Given its centrality, it is important to be able to characterize multipartite entanglement in materials.

Although there are many approaches for quantifying bipartite entanglement in synthetic quantum systems [8–20], most of these are impractical for solid-state quantum materials, due to either the large number of atoms in such materials or the lack of fine-scale control. Entanglement in magnetic materials between spin pairs can be inferred from magnetic susceptibility [21–25], magnetic specific heat [26], or the dynamical spin structure factor

[27–29]. A more general approach both capable of detecting arbitrary amounts of multipartite entanglement and that is potentially compatible with a variegated set of experimental solid state probes is the quantum Fisher information (QFI) [30]. The QFI is a concept from quantum metrology [3, 31–33] that pertains to the probability distribution of measurements and the corresponding parameter estimation in a multiparticle quantum system. If the precision of a parameter estimation exceeds the classical limit, then it can be deduced that the system must have multipartite entanglement [34–38]. As shown in Ref. [36], the QFI can be deduced from appropriately weighted energy-integrals of dynamical susceptibilities. This approach depends on the operator associated with the susceptibility being both Hermitian and having bosonic statistics. Since the spin operator fulfills this criterion, the formulae in Ref. [36] can be directly applied to inelastic neutron scattering, and this has been successfully used to detect entanglement in quasi-one-dimensional quantum magnets [30, 39, 40].

RIXS is a fast-evolving experimental technique that can probe charge, spin, and orbital degrees of freedom [41–44]. Given its flexibility to probe multiple degrees of freedom and its ability to measure very small sample volumes and in ultrafast pump-probe modalities, it offers exciting possibilities to expand the frontier of entanglement metrology in quantum materials [44–46]. However, while the RIXS intensity is bosonic, it is non-Hermitian, so Ref. [36]’s formalism cannot be directly applied. One way to circumvent this difficulty is to convert the RIXS intensity into an approximate estimate for the dynamical

* tren@bnl.gov

† yshen@iphy.ac.cn

‡ mdean@bnl.gov

§ rmk@bnl.gov

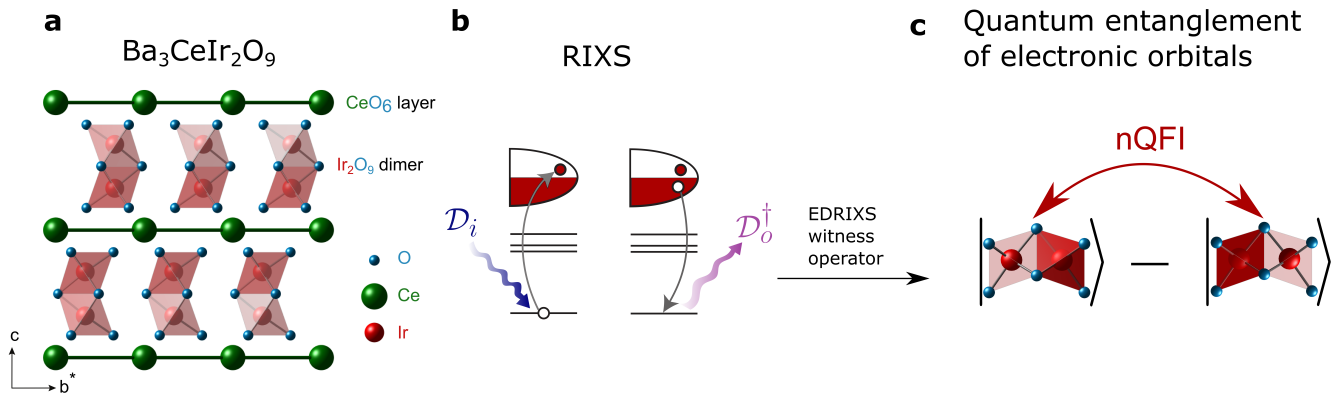


FIG. 1. **Witnessing orbital entanglement using RIXS.** **a**, The crystal structure of $\text{Ba}_3\text{CeIr}_2\text{O}_9$ is shown with the dimer units highlighted in red, which host Ir $5d$ orbitals. **b**, In this letter, we develop a joint experimental-theoretical method to obtain an orbital entanglement witness from the RIXS intensity, which probes the material through a scattering process involving the absorption (\mathcal{D}_i) and the subsequent emission (\mathcal{D}_0^\dagger) of x-rays shown as wavy blue and purple lines. **c**, We first obtain the witness operator from the RIXS intensity using the numerical codebase EDRIXS and subsequently obtain the normalized quantum Fisher information (nQFI) for detection of the quantum entanglement.

spin structure factor [47].

The key result of this letter is that we show how to extend Ref. [36]’s formalism to cover non-Hermitian operators and use it to directly formulate an entanglement witness that exploits the full complexity of the RIXS response. We use this theoretical advance to convert measured RIXS intensities of $\text{Ba}_3\text{CeIr}_2\text{O}_9$ to the normalized QFI. This material features face-sharing Ir octahedra, which makes it an ideal test case for detecting a prototypical two-partite entanglement between its t_{2g} electronic orbitals. An overview of this process is illustrated in Fig. 1.

DESIGNING RIXS AS AN ENTANGLEMENT WITNESS

Entanglement: Quantum entanglement is a property of the many-body wave function of a quantum system. To define multipartite entanglement [48, 49], first consider a pure state $\rho = |\psi\rangle\langle\psi|$ of a N -site system. The state is said to be m -separable if one can write the state as a product of states ρ_j involving $m_j \leq m$ sites:

$$\rho = \otimes_{j=1}^M \rho_j, \quad \sum_{j=1}^M m_j = N. \quad (1)$$

If the state cannot be further factorized into smaller pieces, it is said to possess m -partite entanglement. A mixed, i.e., thermal, state, $\rho = \sum_i \rho_i |\psi_i\rangle\langle\psi_i|$, is said to possess m -partite entanglement if the maximally entangled wavefunction, $|\psi_i\rangle$, in the mixture has m -partite entanglement [30, 34, 35, 50, 51]. The physical consequence of entanglement is that a measurement of one site in the system, represented by the action of an operator on that site, necessarily affects the other entangled sites.

Quantum Fisher information: The quantum Fisher information (QFI) provides a way to connect bounds on the multipartite entanglement with spectroscopic probes that can be measured experimentally. The QFI, $F_Q(\rho, \hat{A})$, governs the sensitivity of the quantum density matrix ρ to unitary rotations $U^\dagger \rho U$, $U = e^{i\theta \hat{A}}$, defined in terms of a Hermitian operator \hat{A} [35, 52]. The variance by which the parameter θ can be determined by a single measurement is given by $(\Delta\theta)^2 \geq F_Q(\rho, \hat{A})^{-1}$.

The QFI is expressible in terms of the response function relative to the operator \hat{A} , the key observation of Ref. [36]:

$$F_Q(\rho, \hat{A}) = 4 \int_0^\infty d\omega \tanh\left(\frac{\beta\omega}{2}\right) \chi''_{AA}(\omega), \quad (2)$$

where $\chi''_{AA}(\omega)$ is the imaginary part of the retarded correlation function

$$\chi''_{AA}(\omega) = \text{Im} \left[i \int_0^\infty \frac{dt}{\pi} e^{i\omega t} \text{Tr} \left(\rho \left[\hat{A}(t), \hat{A}(0) \right] \right) \right]. \quad (3)$$

It has been shown that if the QFI exceeds a certain bound [34, 50, 51, 53], the state is guaranteed to have a certain level of multipartite entanglement. In metrological terms, this means that the presence of multipartite entanglement makes measurements of the parameter, θ , more accurate than would be possible if the state were purely classical without any entanglement. To quantify this bound, we assume that the operator \hat{A} is a sum over local operators defined at each site of the system $\hat{A} = \sum_{i=1}^N \hat{A}_i$, and we denote the maximum and minimum eigenvalues of \hat{A}_i as $a_{i,\max}$ and $a_{i,\min}$ respectively. If the QFI satisfies

$$\frac{F_Q(\rho, \hat{A})}{\sum_{i=1}^N (\Delta a_i)^2} > m, \quad \Delta a_i = a_{i,\max} - a_{i,\min}, \quad (4)$$

then the state ρ is guaranteed to have $(m+1)$ -partite entanglement. The left-hand side of the inequality in Eq. (4) is referred to as the normalized QFI (nQFI).

Exploiting this connection between $F_Q(\rho, \hat{A})$ and χ''_{AA} , the multipartite entanglement of quasi-1D quantum magnets was determined from neutron scattering measurements of the dynamic spin structure factor, i.e., $\hat{A} = \hat{S}$ [30, 39, 40]. The key challenge of applying this approach to RIXS is that the relevant operator \hat{A} for RIXS is not Hermitian so Ref. [36]'s formalism cannot be straightforwardly employed.

RIXS as an entanglement witness: In RIXS, x-rays with energy $\hbar\omega_{\text{in}}$, momentum $\hbar\mathbf{k}_i$, and polarization ϵ_i excite a core electron to the valence band. The resulting core hole is then refilled by a valence electron and an outgoing photon with energy loss ω , momentum $\hbar\mathbf{k}_o$ and polarization ϵ_o is emitted. The corresponding RIXS intensity is described by the the Kramers-Heisenberg formula [41, 44, 54]

$$I_{\text{RIXS}}(\omega_{\text{in}}, \omega, \mathbf{k}_i, \mathbf{k}_o, \epsilon_i, \epsilon_o) = \sum_g \frac{e^{-\beta E_g}}{\sum_{g'} e^{-\beta E_{g'}}} \sum_f \sum_n \left| \frac{\langle f | \hat{D}_o^\dagger | n \rangle \langle n | \hat{D}_i | g \rangle}{\omega_{\text{in}} - E_n + E_g + i\Gamma_c} \right|^2 \frac{\Gamma/\pi}{(\omega - E_f + E_g)^2 + \Gamma^2}. \quad (5)$$

Here, $|g\rangle$ and $|f\rangle$ are the initial and final eigenstates of the Hamiltonian without a core hole \hat{H}_0 , with eigenvalues of E_g and E_f , respectively. $|n\rangle$ is the eigenstate of the Hamiltonian with the core hole present \hat{H}_n , with eigenvalue E_n . $T = (k_B\beta)^{-1}$ is the sample temperature. Γ is the inverse lifetime of the final state, Γ_c is the inverse lifetime of the core-hole state. $\hat{D}_i(\mathbf{k}_i, \epsilon_i)$ and $\hat{D}_o(\mathbf{k}_o, \epsilon_o)$ are the dipole transition operators [55]. For experiments that do not discriminate the final-state polarization, we also need to sum over ϵ_o in Eq. (5).

Inspecting Eq. (5), we identify the RIXS operator \hat{A}_R^\dagger via its matrix elements:

$$\langle f, \epsilon_o | \hat{A}_R^\dagger | g, \epsilon_i \rangle = \sum_n \frac{\langle f | \hat{D}_o^\dagger(\epsilon_o) | n \rangle \langle n | \hat{D}_i(\epsilon_i) | g \rangle}{\omega_{\text{in}} - E_n + E_g + i\Gamma_c}. \quad (6)$$

Then the RIXS intensity can be written as

$$I_{\text{RIXS}}(\omega) = \frac{\chi''_{A_R A_R^\dagger}(\omega)}{1 - e^{-\beta\omega}}, \quad (7)$$

where we have omitted the dependencies on the incoming and outgoing photons for notational conciseness.

To convert $I_{\text{RIXS}}(\omega)$ into a witness of entanglement despite the non-Hermiticity of \hat{A}_R , we consider instead the real and imaginary parts of the RIXS operator:

$$\hat{A}_{R,\text{Re}} = \frac{1}{2} (\hat{A}_R + \hat{A}_R^\dagger), \quad \hat{A}_{R,\text{Im}} = \frac{1}{2i} (\hat{A}_R - \hat{A}_R^\dagger). \quad (8)$$

We can thus define the QFI for both:

$$F_Q(\rho, \hat{A}_{R,\text{Re}}), \quad F_Q(\rho, \hat{A}_{R,\text{Im}}). \quad (9)$$

Each of these QFI's individually is not connected to a spectroscopy that can be experimentally measured. However, as one of our key results, the sum of the two is related to the RIXS intensity $I_{\text{RIXS}}(\omega)$ measured at all frequencies, both positive and negative:

$$\begin{aligned} & F_Q(\rho, \hat{A}_{R,\text{Re}}) + F_Q(\rho, \hat{A}_{R,\text{Im}}) \\ &= 2 \int_0^\infty d\omega \tanh\left(\frac{\beta\omega}{2}\right) \left[\chi''_{A_R A_R^\dagger}(\omega) + \chi''_{A_R^\dagger A_R}(\omega) \right] \\ &= 2 \int_{-\infty}^\infty d\omega \tanh\left(\frac{\beta\omega}{2}\right) (1 - e^{-\beta\omega}) I_{\text{RIXS}}(\omega). \end{aligned} \quad (10)$$

Akin to Eq. (4), if this QFI sum satisfies

$$\frac{F_Q(\rho, \hat{A}_{R,\text{Re}}) + F_Q(\rho, \hat{A}_{R,\text{Im}})}{\sum_{i=1}^N \left[(\Delta a_{i,\text{Re}})^2 + (\Delta a_{i,\text{Im}})^2 \right]} > m, \quad (11)$$

then our material has at least $(m+1)$ -partite entanglement. Here we have written our RIXS operator as a sum over sites in the system, $\hat{A}_R^\dagger = \sum_{i=1}^N \hat{A}_{R,i}^\dagger$, where $\hat{A}_{R,i}^\dagger$ excites/deexcites a core hole on site i . In the following section, we will show how to obtain these necessary quantities in the case of dimer iridates, which are attractive in that they offer a prototypical bipartite entanglement between the neighboring Ir atoms.

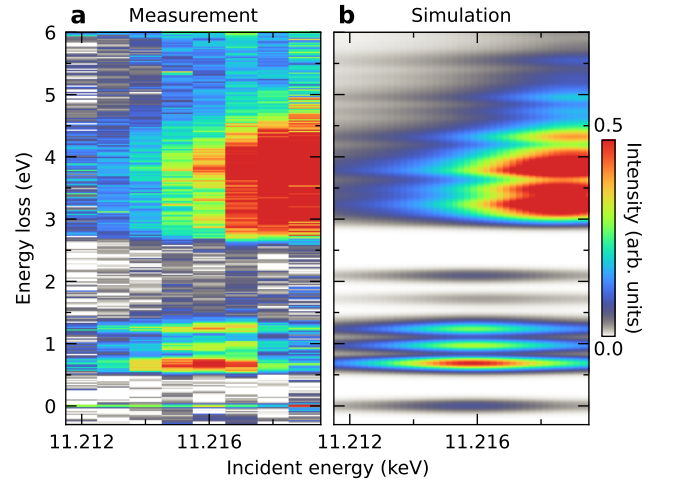


FIG. 2. Comparison of the incident energy dependence of the RIXS spectra between measurement and simulation. **a**, Measured RIXS spectra with varying incident energy at fixed momentum transfer $Q = (-0.5, 0, 18.94)$ in reciprocal lattice units (r.l.u.). The signals below 2 eV energy loss correspond to intra- t_{2g} transitions while the ones above 2 eV mainly come from inter- t_{2g} - e_g transitions. **b**, Calculated incident-energy-dependent RIXS spectra at the same fixed momentum transfer.

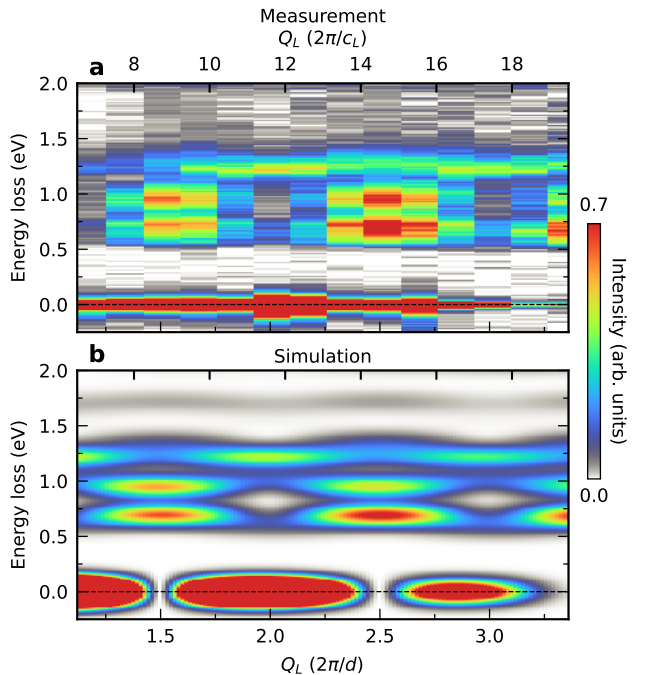


FIG. 3. **Comparison of the L dependence of the RIXS spectra between measurement and simulation.** **a**, Measured L -dependent RIXS spectra showing periodic modulation, where the momentum transfer is $Q = (-0.5, 0, L)$ r.l.u., and the incident energy $\hbar\omega_{\text{in}}$ is fixed to 11.216 keV. Only the intra- t_{2g} transitions are presented since they are the dominating signals at this particular incident energy. **b**, Calculated L -dependent RIXS spectra at the same fixed incident energy. Q_L is the momentum transfer along the L direction. For convenience, the same momentum scale is displayed in two units. On top, we use units of $2\pi/c_L$ where c_L is the unit cell lattice constant along L direction. On bottom, we use units of $2\pi/d$, where d is the distance between the two dimers along the L direction.

CASE STUDY IN IRIDATE DIMER MATERIALS

As shown in Fig. 1, $\text{Ba}_3\text{CeIr}_2\text{O}_9$ features two Ir sites in its basic structural motif hosting ten $5d$ electrons between them. Ir L -edge RIXS involves interference between processes that create a core hole at either one of these sites and can be used to formulate a RIXS witness for the simplest form of multiparticle entanglement — that of bipartite entanglement — between these sites.

To apply our QFI metrology, we need an estimate for the single site eigenvalue spread, $\Delta a_{i, \text{Re}/\text{Im}}$. To obtain this, we need to model the material-specific RIXS operator. This is done using the numerical toolkit EDRIXS, we tune four material parameters (one crystal field splitting parameter κ and three hopping integrals $V_{dd\sigma}$, $V_{dd\pi}$, $V_{dd\delta}$, see Table I, Refs. 56 and 57) together with a single overall scale factor to reproduce the experimentally measured RIXS intensity. The results are shown in Figs. 2, 3, and 4. It can be seen from the figures that the constructed

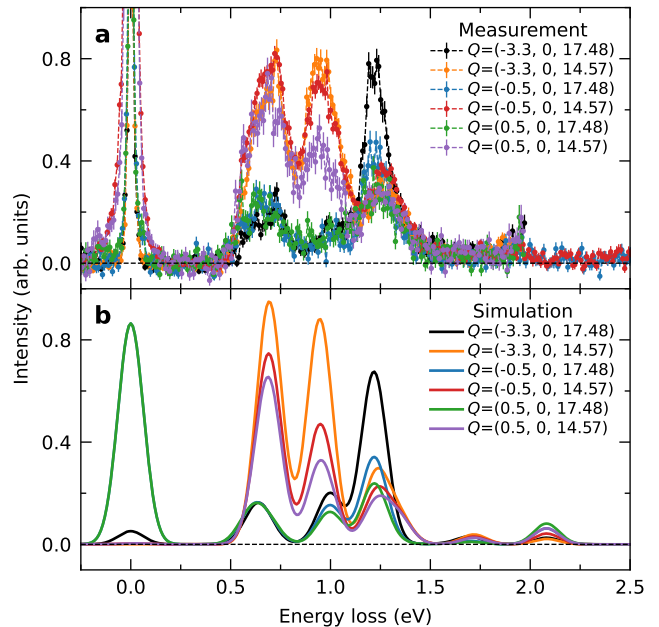


FIG. 4. **Comparison of RIXS spectra between measurement and simulation at representative momentum transfers.** **a**, Representative RIXS spectra at the indicated momentum transfers in r.l.u., and the incident energy $\hbar\omega_{\text{in}}$ is fixed to 11.216 keV. Only the intra- t_{2g} transitions are presented since they are the dominant signal at this particular incident energy. **b**, Calculated RIXS spectra at the same momentum transfers and the same fixed incident energy. The model faithfully reproduces the trends seen in the experiment. The first two inelastic features around 0.7 and 0.9 eV are strong at $L = 14.57$ and weak at $L = 17.48$ due to constructive or destructive inter-site interference, respectively. The feature around 1.2 eV has different symmetry and the opposite trend in L .

RIXS operator indeed reproduces the essential features of the measured RIXS intensity, especially the major RIXS peaks below the energy loss gap around 2 eV, and these RIXS peaks are the dominant signal for incident energy around 11.216 keV.

To better understand the electronic characteristics of these major RIXS peaks at low energy losses, we trace the evolution of the eigenenergies with the spin-orbit coupling (SOC), the crystal electric field (CEF) due to trigonal distortion, and the hopping amplitude. This is shown in Fig. 5, where we can see that the ground state lies in the t_{2g} orbital manifold, and the excitations below 2 eV are primarily intra- t_{2g} .

With the RIXS operator at hand, we can calculate the nQFI from Eqs. (11) and (10) for different incident energies and different momentum transfers, which correspond to different choices of entanglement witnesses. To do this, we also use the model verified on the energy loss data to compute $I_{\text{RIXS}}(\omega)$ for $\omega < 0$. This is necessary because such processes are thermally suppressed so that they cannot be seen directly in the spectra but,

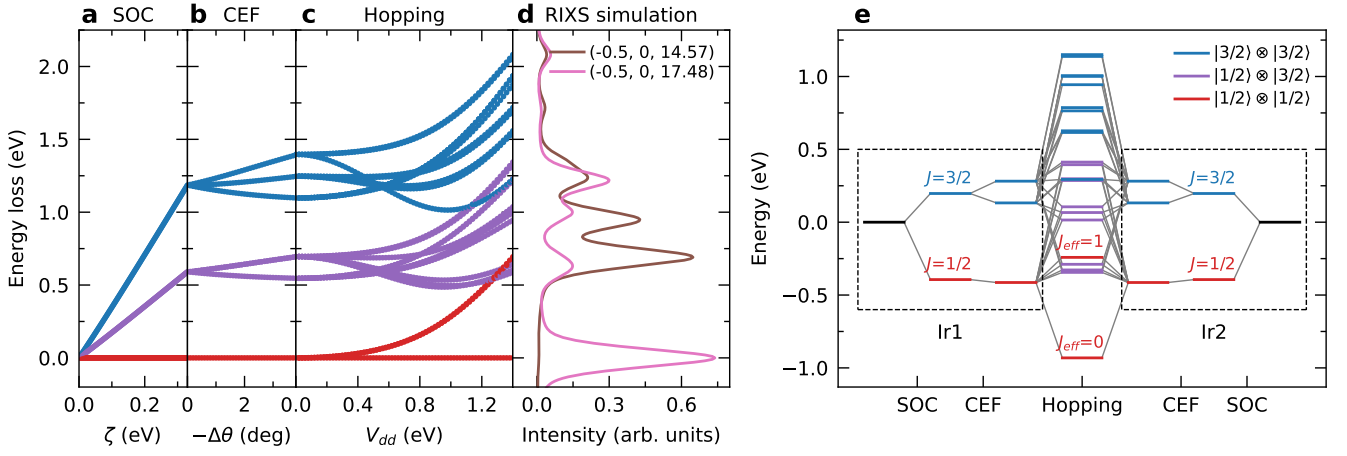


FIG. 5. **Tracing the evolution of the eigenenergies from ED calculations.** **a**, For a single Ir^{4+} ion with octahedral coordination, the degenerate t_{2g} orbital manifold is split into $J = 1/2$ and $J = 3/2$ multiplets due to the strong spin-orbit coupling (SOC). For two Ir^{4+} ions, these make three combinations of $|1/2\rangle \otimes |1/2\rangle$ (red), $|1/2\rangle \otimes |3/2\rangle$ (purple), and $|3/2\rangle \otimes |3/2\rangle$ (blue). **b**, The inclusion of trigonal distortion induced crystal electric field (CEF) leads to the splitting of the $J = 3/2$ state. **c**, The inter-atomic hopping mixes and rearranges all the states which contribute to the RIXS spectra in **d**. **e**, The orbital-energy diagram summarizing **a-c** indicates that the ground state of the system is a $J_{\text{eff}} = 0$ singlet state originating from the two interacting $J = 1/2$ Ir doublets and the strongest RIXS peak at around 0.7 eV corresponds to the $J_{\text{eff}} = 1$ triplet state.

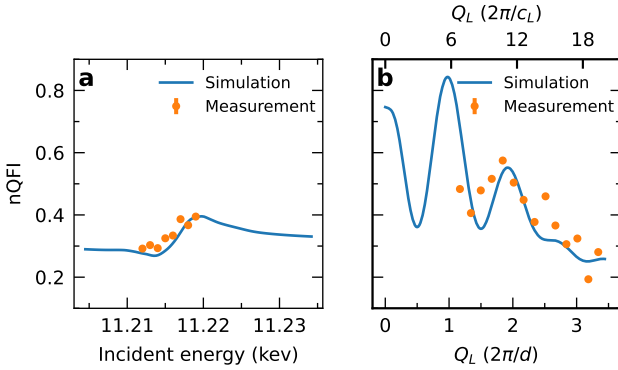


FIG. 6. **The entanglement witness - comparison between simulation and measurement.** **a** is for fixed momentum transfer at $Q = (-0.5, 0, 18.94)$ r.l.u and different incident energies; **b** is for fixed incident energy at $\hbar\omega_{\text{in}} = 11.216$ keV and different momentum transfers $Q = (-0.5, 0, L)$ r.l.u.

the weighted integral in Eq. (10) involves a countervailing factor causing them to contribute appreciably to the entanglement estimate.

Firstly, we perform this calculation with the same incident energies and momentum transfers as the existing experimental data, as plotted in Fig. 6. We can see that a large momentum transfer severely suppresses the nQFI across a range of incident energies, thus a suitable entanglement witness should favor relatively small momentum transfers and wavevectors that involve constructive interference between the sites. On the other hand, if the incident energy is fixed to around 11.216 keV, where the intra- t_{2g} transitions dominates and the inter- t_{2g} - e_g

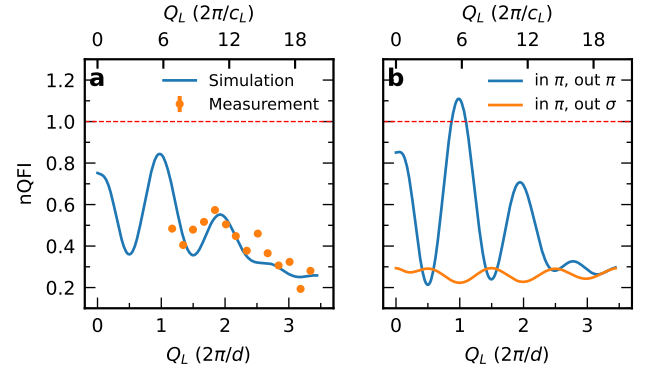


FIG. 7. **Witness measurements with scattered x-ray polarization discrimination can detect entanglement.** **a** reproduces the right panel of Fig. 6; **b** is for the same setup as **a** but with final state polarization discrimination. The red dashed line is the nQFI threshold for 2-partite entanglement. The legend in the right panel documents the polarizations for the final state (out) and incident beam (in), where the π polarization is in the incident plane, σ polarization is out of the incident plane.

transitions are suppressed, the resulting nQFI still cannot exceed the threshold for 2-partite entanglement, irrespective of the choice of momentum transfer. We tested whether downfolding the model to the t_{2g} manifold only would give us the desired enhancement of the nQFI to the extent where the 2-partite entanglement threshold can be exceeded, but it cannot.

Following the typical practice for hard x-ray RIXS, our experiments used fixed incident x-ray polarization, but did not discriminate the scattered x-ray polarization. We

account for this by enlarging the Hilbert space in constructing the RIXS operator [see Eq. (6)] and exclude polarization as an extra witness selector. Still, we can use the tuned parameters to simulate the situation that can discriminate the final-state polarization, where we exclude the polarization from the Hilbert space and include it as another witness selector. The results for the same incident energy and momentum transfers as the existing experimental data are shown in Fig. 7. We can see that the nQFI is substantially enhanced by measuring RIXS intensity at the same polarization as the incident beam, which can eventually exceed the threshold for 2-partite entanglement at relatively small momentum transfers. In contrast, the nQFI corresponding to a final state polarization orthogonal to the incident beam is substantially suppressed, making the nQFI with final state summation over polarizations inefficient in detecting the entanglement.

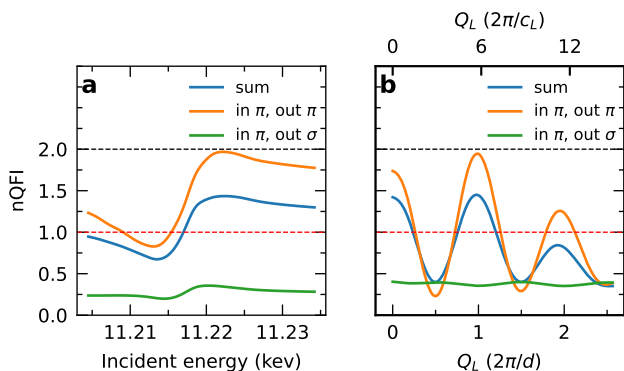


FIG. 8. **Using higher incident energies allows entanglement detection.** **a** is for fixed momentum transfer at $Q = (-0.5, 0, 6)$ r.l.u; **b** is for fixed incident energy at $\hbar\omega_{\text{in}} = 11.220$ keV and different momentum transfers $Q = (-0.5, 0, L)$ r.l.u. Both summation (blue) and discrimination of the scattered x-ray polarizations (orange and green) are shown. The red dashed line is the nQFI threshold for 2-partite entanglement, and the black dashed line is the upper bound for nQFI in a dimer system.

Although the discrimination of the final state polarization provides us a handle to enhance the efficiency of the entanglement detection using RIXS, it requires specialized experimental equipment. It is then desirable to find an alternative solution that has less stringent requirements on the equipment. Indeed, as can be observed from Fig. 2, there is more inelastic intensity if the incident energy is tuned upward toward 11.220 keV. Although these intensities come from the inter- t_{2g} - e_g transitions, they still play an equally important role as the intra- t_{2g} transitions, according to Eq. (10). We performed the corresponding calculations, and the results are shown in Fig. 8. Indeed, by tuning the incident energy around 11.220 keV, we can find efficient entanglement witnesses across a range of relatively small momentum transfers. As a comparison, we also performed the corresponding

calculation that discriminates the final state polarizations, and the results are also shown in Fig. 8. We can see that the same final state polarization as the incident beam can push the nQFI toward the upper bound for the 2-partite entanglement, the natural limit for the dimer system under consideration.

CONCLUSION AND DISCUSSION

In this letter, we have generalized the protocol of using the QFI for entanglement detection to the case with a non-Hermitian operator, and applied it to iridate dimer systems using RIXS as the entanglement witness. Surprisingly, we find that a large fraction of the measurement phase space cannot detect any entanglement. We predict, however, that measurements at lower momentum transfer, higher incident energy resonant with the e_g manifold, or with scatter-beam polarization analysis could detect entanglement. It is unexpected that to detect the entanglement between the t_{2g} orbitals, a more efficient choice would be to include the inter- t_{2g} - e_g transitions. This reflects the complexity of the formula for QFI in Eq. (10). Another insight is that strategic choices for the x-ray polarization can be used to increase the effectiveness of the entanglement witness. This gives us a hint that we would benefit from designing and choosing an entanglement witness with a higher degree of tunability.

Our result constitutes the first approach to experimentally detect orbital electronic quantum entanglement in a real quantum material. Experimental detection of quantum entanglement has been previously reported only for synthetic few-body systems [8, 9, 11–14, 17–20, 58], and for bosonic degrees of freedom in low-dimensional quantum magnets [21–30, 39, 40, 59]. Besides, quantum entanglement detection has been simulated theoretically for bosonic degrees of freedom in several 1D strongly correlated model systems out of equilibrium [47, 60]. We have generalized the protocol of using the QFI for entanglement detection to non-Hermitian operators, enabling the direct detection of electronic quantum entanglement. As a result, our protocol can utilize other entanglement witnesses, such as the RIXS intensity considered in this letter, which enlarges the class of quantum materials whose quantum entanglement is subject to experimental detection. This is particularly helpful in the case of the iridate dimers, where inelastic neutron scattering is impractical.

Apart from the results for $\text{Ba}_3\text{CeIr}_2\text{O}_9$ presented above in the main text, we have also performed the same analysis for $\text{Ba}_3\text{TaIr}_2\text{O}_9$. The results are presented in the Supplementary Information and are consistent with those for $\text{Ba}_3\text{CeIr}_2\text{O}_9$ [55], confirming the generality of the applicability of our protocol.

Apart from the site degree of freedom, there are also spin and orbital degrees of freedom involved in the iridate dimers. RIXS offers possibilities for separating different orbitals via specific selection of energies. We tested this

for the current case of $\text{Ba}_3\text{CeIr}_2\text{O}_9$, but determined that the t_{2g} - e_g mixing is too large.

Overall, our work delivers a new approach for entanglement detection with RIXS, which offers routes to new types of entanglement metric for different degrees of freedom. Given the flexibility of RIXS, this also opens routes to entanglement measurements in thin films and in non-equilibrium settings.

METHODS

Sample synthesis: Single crystals of $\text{Ba}_3\text{CeIr}_2\text{O}_9$ were grown using the melt-solution technique in BaCl_2 flux. Stoichiometric quantities of BaCO_3 , CeO_2 , and IrO_2 were used as starting materials. After growth, the crystals were mechanically separated from the flux and washed with water to remove flux residues. The crystal possesses a $P6_3/mmc$ (No. 194) space group with lattice constants of $a = b = 5.9035(9)$ Å, $c = 14.715(3)$ Å, $\alpha = \beta = 90^\circ$ and $\gamma = 120^\circ$ [56]. Within this crystal structure, the Ir atoms forming the dimer are separated by $d = 2.5361(7)$ Å along the sample c -axis direction.

RIXS measurements: The RIXS experiments were performed at the 27-ID-B endstation of the Advanced Photon Source at Argonne National Laboratory. We used a spherically bent Si (844) diced analyzer and a Si (844) channel cut monochromator. The overall energy resolution was around 42 meV. The sample was mounted with its H and L reciprocal lattice vectors in the horizontal scattering plane and horizontally (π)-polarized incident x-rays were used. Data were collected at 9 K unless otherwise specified. For all the resonant inelastic x-ray scattering (RIXS) data presented in the manuscript, a constant background has been subtracted using the energy-gain side followed by self-absorption correction for each spectrum.

Exact diagonalization calculations: The ED calculations for $\text{Ba}_3\text{CeIr}_2\text{O}_9$ were performed using the EDRIXS software based on a two-Ir-site cluster [54]. For the Hamiltonian, we explicitly include the onsite Coulomb interactions and spin orbit coupling, which depend primarily on the atomic properties of Ir and are therefore fixed to $U = 3$ eV, $J_H = 0.4$ eV and $\zeta = 0.33$ eV ac-

ording to previous experience. The octahedral crystal field splitting can be seen directly in the different resonant energies of the t_{2g} and e_g manifolds and is fixed to $10D_q = 3.5$ eV. The trigonal distortion is included through the approach described in Ref. 57, in which θ , the Ir-Ir-O angle, is fixed to the experimental value of the material, leaving κ the only tunable parameter. The direct hoppings between the neighboring Ir atoms are described by three Slater-Koster parameters, $V_{dd\sigma}$, $V_{dd\pi}$ and $V_{dd\delta}$, all of them are treated as tunable parameters. Regarding the Hartree-Fock basis, we consider $t_{2g}^1 e_g^0$ and $t_{2g}^0 e_g^1$ configurations only considering the negligible double e_g occupancy. The richly-structured experimental data allow us to find a combination of parameters that can reproduce the collected RIXS data, the full list of which is presented in Table I. The RIXS spectra are calculated using the Kramers-Heisenberg formula in the dipole approximation with the experimental geometry explicitly considered. The calculations overall show excellent agreement with only four tunable parameters.

Our model is similar to that used in Ref. 56 but with the key improvement to include e_g occupancy in addition to t_{2g} occupancy. It has been discovered that spin orbital coupling will mix t_{2g} and e_g levels up to 20% [61].

DATA AVAILABILITY

The RIXS data generated in this study have been deposited in the Zenodo database under accession code [to be assigned].

CODE AVAILABILITY

The exact diagonalization is done using the codebase EDRIXS [54]. The code used in this study is available from the authors upon reasonable request.

REFERENCES

-
- [1] E. Chitambar and G. Gour, Quantum resource theories, *Rev. Mod. Phys.* **91**, 025001 (2019).
 - [2] A. Piveteau, J. Pauwels, E. Håkansson, S. Muhammad, M. Bourennane, and A. Tavakoli, Entanglement-assisted quantum communication with simple measurements, *Nature Communications* **13**, 7878 (2022).
 - [3] V. Giovannetti, S. Lloyd, and L. Maccone, Advances in quantum metrology, *Nature Photonics* **5**, 222 (2011).
 - [4] C. L. Degen, F. Reinhard, and P. Cappellaro, Quantum sensing, *Rev. Mod. Phys.* **89**, 035002 (2017).
 - [5] D. P. García, J. Cruz-Benito, and F. J. García-Peñalvo, Systematic literature review: Quantum machine learning and its applications (2022), [arXiv:2201.04093](https://arxiv.org/abs/2201.04093) [quant-ph].
 - [6] O. S. Magaña-Loaiza and R. W. Boyd, Quantum imaging and information, *Reports on Progress in Physics* **82**, 124401 (2019).
 - [7] P.-A. Moreau, E. Toninelli, T. Gregory, and M. J. Padgett, Imaging with quantum states of light, *Nature Reviews Physics* **1**, 367 (2019).
 - [8] H. Häffner, W. Hänsel, C. F. Roos, J. Benhelm, D. Chekhalkar, M. Chwalla, T. Körber, U. D. Rapol, M. Riebe,

TABLE I. Full list of parameters used in the ED calculations for $\text{Ba}_3\text{CeIr}_2\text{O}_9$. The CEF parameters such as θ and κ are defined in Ref. 57. Here, ζ is the spin orbit coupling parameter for the Ir $5d$ orbitals while the one for the $2p$ core orbitals is fixed to the atomic value 1140.332 eV. The inverse core-hole lifetime is set to the atomic value 2.47 eV and the final-state energy loss spectra are broadened using a Gaussian function with a full-width at half-maximum of 0.15 eV. All parameters except θ and κ are in units of eV.

Crystal field splitting and spin orbit coupling				Hopping integrals		
$10D_q$	θ	κ	ζ	$V_{dd\sigma}$	$V_{dd\pi}$	$V_{dd\delta}$
3.5	50.86	0.1	0.33	-1.40	-0.66	0.05
Core-hole potential				On-site Coulomb interactions		
F_{dp}^0	F_{dp}^2	G_{dp}^1	G_{dp}^3	F_{dd}^0	F_{dd}^2	F_{dd}^4
2.574	0.927	0.800	0.475	2.543	3.446	2.154

- P. O. Schmidt, C. Becher, O. Gühne, W. Dür, and R. Blatt, Scalable multiparticle entanglement of trapped ions, *Nature* **438**, 643 (2005).
- [9] P. Jurcevic, B. P. Lanyon, P. Hauke, C. Hempel, P. Zoller, R. Blatt, and C. F. Roos, Quasiparticle engineering and entanglement propagation in a quantum many-body system, *Nature* **511**, 202 (2014).
- [10] G. Tóth, C. Knapp, O. Gühne, and H. J. Briegel, Spin squeezing and entanglement, *Phys. Rev. A* **79**, 042334 (2009).
- [11] J. Estève, C. Gross, A. Weller, S. Giovanazzi, and M. K. Oberthaler, Squeezing and entanglement in a Bose-Einstein condensate, *Nature* **455**, 1216 (2008).
- [12] C. Gross, T. Zibold, E. Nicklas, J. Estève, and M. K. Oberthaler, Nonlinear atom interferometer surpasses classical precision limit, *Nature* **464**, 1165 (2010).
- [13] T. Fukuhara, S. Hild, J. Zeiher, P. Schauß, I. Bloch, M. Endres, and C. Gross, Spatially resolved detection of a spin-entanglement wave in a Bose-Hubbard chain, *Phys. Rev. Lett.* **115**, 035302 (2015).
- [14] M. Cramer, A. Bernard, N. Fabbri, L. Fallani, C. Fort, S. Rosi, F. Caruso, M. Inguscio, and M. B. Plenio, Spatial entanglement of Bosons in optical lattices, *Nature Communications* **4**, 2161 (2013).
- [15] J. Cardy, Measuring entanglement using quantum quenches, *Phys. Rev. Lett.* **106**, 150404 (2011).
- [16] D. A. Abanin and E. Demler, Measuring entanglement entropy of a generic many-body system with a quantum switch, *Phys. Rev. Lett.* **109**, 020504 (2012).
- [17] A. J. Daley, H. Pichler, J. Schachenmayer, and P. Zoller, Measuring entanglement growth in quench dynamics of Bosons in an optical lattice, *Phys. Rev. Lett.* **109**, 020505 (2012).
- [18] N. M. Linke, S. Johri, C. Figgatt, K. A. Landsman, A. Y. Matsuura, and C. Monroe, Measuring the Rényi entropy of a two-site Fermi-Hubbard model on a trapped ion quantum computer, *Phys. Rev. A* **98**, 052334 (2018).
- [19] T. Brydges, A. Elben, P. Jurcevic, B. Vermersch, C. Maier, B. P. Lanyon, P. Zoller, R. Blatt, and C. F. Roos, Probing Rényi entanglement entropy via randomized measurements, *Science* **364**, 260 (2019).
- [20] I. Pitsios, L. Banchi, A. S. Rab, M. Bentivegna, D. Caprara, A. Crespi, N. Spagnolo, S. Bose, P. Mataloni, R. Osellame, and F. Sciarrino, Photonic simulation of entanglement growth and engineering after a spin chain quench, *Nature Communications* **8**, 1569 (2017).
- [21] S. Ghosh, T. F. Rosenbaum, G. Aeppli, and S. N. Coppersmith, Entangled quantum state of magnetic dipoles, *Nature* **425**, 48 (2003).
- [22] Č. Brukner, V. Vedral, and A. Zeilinger, Crucial role of quantum entanglement in bulk properties of solids, *Phys. Rev. A* **73**, 012110 (2006).
- [23] T. G. Rappoport, L. Ghivelder, J. C. Fernandes, R. B. Guimarães, and M. A. Continentino, Experimental observation of quantum entanglement in low-dimensional spin systems, *Phys. Rev. B* **75**, 054422 (2007).
- [24] D. Das, H. Singh, T. Chakraborty, R. K. Gopal, and C. Mitra, Experimental detection of quantum information sharing and its quantification in quantum spin systems, *New Journal of Physics* **15**, 013047 (2013).
- [25] S. Sahling, G. Remenyi, C. Paulsen, P. Monceau, V. Saligrama, C. Marin, A. Revcolevschi, L. P. Regnault, S. Raymond, and J. E. Lorenzo, Experimental realization of long-distance entanglement between spins in antiferromagnetic quantum spin chains, *Nature Physics* **11**, 255 (2015).
- [26] H. Singh, T. Chakraborty, D. Das, H. S. Jeevan, Y. Tokiwa, P. Gegenwart, and C. Mitra, Experimental quantification of entanglement through heat capacity, *New Journal of Physics* **15**, 113001 (2013).
- [27] M. B. Stone, W. Tian, M. D. Lumsden, G. E. Granroth, D. Mandrus, J.-H. Chung, N. Harrison, and S. E. Nagler, Quantum spin correlations in an organometallic alternating-sign chain, *Phys. Rev. Lett.* **99**, 087204 (2007).
- [28] T. Vértesi and E. Bene, Thermal entanglement in the nanotubular system $\text{Na}_2\text{V}_3\text{O}_7$, *Phys. Rev. B* **73**, 134404 (2006).
- [29] N. B. Christensen, H. M. Rønnow, D. F. McMorrow, A. Harrison, T. G. Perring, M. Enderle, R. Coldea, L. P. Regnault, and G. Aeppli, Quantum dynamics and entanglement of spins on a square lattice, *Proceedings of the National Academy of Sciences* **104**, 15264 (2007).
- [30] A. Scheie, P. Laurell, A. M. Samarakoon, B. Lake, S. E. Nagler, G. E. Granroth, S. Okamoto, G. Alvarez, and D. A. Tennant, Witnessing entanglement in quantum magnets using neutron scattering, *Phys. Rev. B* **103**, 224434 (2021).
- [31] C. W. Helstrom, Quantum detection and estimation theory, *Journal of Statistical Physics* **1**, 231 (1969).
- [32] S. L. Braunstein and C. M. Caves, Statistical distance and the geometry of quantum states, *Phys. Rev. Lett.* **72**, 3439 (1994).
- [33] G. Tóth and I. Apellaniz, Quantum metrology from a quantum information science perspective, *Journal of Physics A: Mathematical and Theoretical* **47**, 424006 (2014).

- (2014).
- [34] L. Pezzé and A. Smerzi, Entanglement, nonlinear dynamics, and the Heisenberg limit, *Phys. Rev. Lett.* **102**, 100401 (2009).
- [35] L. Pezzé and A. Smerzi, Quantum theory of phase estimation, *arXiv 1411.5164* (2014).
- [36] P. Hauke, M. Heyl, L. Tagliacozzo, and P. Zoller, Measuring multipartite entanglement through dynamic susceptibilities, *Nature Physics* **12**, 778 (2016).
- [37] P. Hyllus, W. Laskowski, R. Krischek, C. Schwemmer, W. Wieczorek, H. Weinfurter, L. Pezzé, and A. Smerzi, Fisher information and multipartite entanglement, *Phys. Rev. A* **85**, 022321 (2012).
- [38] J. Lambert and E. S. Sørensen, Estimates of the quantum fisher information in the $s = 1$ antiferromagnetic heisenberg spin chain with uniaxial anisotropy, *Phys. Rev. B* **99**, 045117 (2019).
- [39] G. Mathew, S. L. L. Silva, A. Jain, A. Mohan, D. T. Adroja, V. G. Sakai, C. V. Tomy, A. Banerjee, R. Goreti, A. V. N., R. Singh, and D. Jaiswal-Nagar, Experimental realization of multipartite entanglement via quantum Fisher information in a uniform antiferromagnetic quantum spin chain, *Phys. Rev. Res.* **2**, 043329 (2020).
- [40] P. Laurell, A. Scheie, C. J. Mukherjee, M. M. Koza, M. Enderle, Z. Tylczynski, S. Okamoto, R. Coldea, D. A. Tennant, and G. Alvarez, Quantifying and controlling entanglement in the quantum magnet Cs_2CoCl_4 , *Phys. Rev. Lett.* **127**, 037201 (2021).
- [41] L. J. P. Ament, M. van Veenendaal, T. P. Devereaux, J. P. Hill, and J. van den Brink, Resonant inelastic x-ray scattering studies of elementary excitations, *Rev. Mod. Phys.* **83**, 705 (2011).
- [42] F. Gel'mukhanov, M. Odelius, S. P. Polyutov, A. Föhlisch, and V. Kimberg, Dynamics of resonant x-ray and Auger scattering, *Rev. Mod. Phys.* **93**, 035001 (2021).
- [43] M. P. M. Dean, Insights into the high temperature superconducting cuprates from resonant inelastic x-ray scattering, *Journal of Magnetism and Magnetic Materials* **376**, 3 (2015).
- [44] M. Mitrano, S. Johnston, Y.-J. Kim, and M. P. M. Dean, Exploring quantum materials with resonant inelastic x-ray scattering (2024).
- [45] M. P. M. Dean, R. S. Springell, C. Monney, K. J. Zhou, J. Pereiro, I. Božović, B. Dalla Piazza, H. M. Rønnow, E. Morenzoni, J. van den Brink, T. Schmitt, and J. P. Hill, Spin excitations in a single La_2CuO_4 layer, *Nat. Mater.* **11**, 850 (2012).
- [46] M. P. M. Dean, Y. Cao, X. Liu, S. Wall, D. Zhu, R. Mankowsky, V. Thampy, X. M. Chen, J. G. Vale, D. Casa, J. Kim, A. H. Said, P. Juhas, R. Alonso-Mori, J. M. Glownia, A. Robert, J. Robinson, M. Sikorski, S. Song, M. Kozina, H. Lemke, L. Patthey, S. Owada, T. Katayama, M. Yabashi, Y. Tanaka, T. Togashi, J. Liu, C. Rayan Serrao, B. J. Kim, L. Huber, C.-L. Chang, D. F. McMorrow, M. Först, and J. P. Hill, Ultrafast energy- and momentum-resolved dynamics of magnetic correlations in the photo-doped Mott insulator Sr_2IrO_4 , *Nat. Mater.* **15**, 601 (2016).
- [47] J. Hales, U. Bajpai, T. Liu, D. R. Baykusheva, M. Li, M. Mitrano, and Y. Wang, Witnessing light-driven entanglement using time-resolved resonant inelastic x-ray scattering, *Nature Communications* **14**, 3512 (2023).
- [48] I. Bengtsson and K. Życzkowski, A brief introduction to multipartite entanglement (2016), *arXiv:1612.07747 [quant-ph]*.
- [49] M. Walter, D. Gross, and J. Eisert, Multi-partite entanglement (2017), *arXiv:1612.02437 [quant-ph]*.
- [50] G. Tóth, Multipartite entanglement and high-precision metrology, *Phys. Rev. A* **85**, 022322 (2012).
- [51] P. Hyllus, W. Laskowski, R. Krischek, C. Schwemmer, W. Wieczorek, H. Weinfurter, L. Pezzé, and A. Smerzi, Fisher information and multipartite entanglement, *Phys. Rev. A* **85**, 022321 (2012).
- [52] B. M. Escher, R. L. de Matos Filho, and L. Davidovich, General framework for estimating the ultimate precision limit in noisy quantum-enhanced metrology, *Nature Physics* **7**, 406 (2011).
- [53] H. Strobel, W. Muessel, D. Linnemann, T. Zibold, D. B. Hume, L. Pezzè, A. Smerzi, and M. K. Oberthaler, Fisher information and entanglement of non-gaussian spin states, *Science* **345**, 424 (2014).
- [54] Y. Wang, G. Fabbris, M. Dean, and G. Kotliar, EdriXs: An open source toolkit for simulating spectra of resonant inelastic x-ray scattering, *Computer Physics Communications* **243**, 151 (2019).
- [55] See Supplementary Information at [URL will be inserted by publisher] for further details of the RIXS transition operators, the relationship between quantum Fisher information and susceptibility, and entanglement metrology in $\text{Ba}_3\text{TaIr}_2\text{O}_9$.
- [56] A. Revelli, M. M. Sala, G. Monaco, P. Becker, L. Bohatý, M. Hermanns, T. C. Koethe, T. Fröhlich, P. Warzanowski, T. Lorenz, S. V. Streltsov, P. H. M. van Loosdrecht, D. I. Khomskii, J. van den Brink, and M. Grüninger, Resonant inelastic x-ray incarnation of Young's double-slit experiment, *Science Advances* **5**, eaav4020 (2019).
- [57] K. I. Kugel, D. I. Khomskii, A. O. Sboychakov, and S. V. Streltsov, Spin-orbital interaction for face-sharing octahedra: Realization of a highly symmetric $\text{SU}(4)$ model, *Phys. Rev. B* **91**, 155125 (2015).
- [58] O. Gühne and G. Tóth, Entanglement detection, *Physics Reports* **474**, 1 (2009).
- [59] A. O. Scheie, E. A. Ghioldi, J. Xing, J. A. M. Paddison, N. E. Sherman, M. Dupont, L. D. Sanjeewa, S. Lee, A. J. Woods, D. Abernathy, D. M. Pajerowski, T. J. Williams, S.-S. Zhang, L. O. Manuel, A. E. Trumper, C. D. Pemmaraju, A. S. Sefat, D. S. Parker, T. P. Devereaux, R. Movshovich, J. E. Moore, C. D. Batista, and D. A. Tennant, Proximate spin liquid and fractionalization in the triangular antiferromagnet KYbSe_2 , *Nature Physics* **20**, 74 (2024).
- [60] D. R. Baykusheva, M. H. Kalthoff, D. Hofmann, M. Claassen, D. M. Kennes, M. A. Sentef, and M. Mitrano, Witnessing nonequilibrium entanglement dynamics in a strongly correlated fermionic chain, *Phys. Rev. Lett.* **130**, 106902 (2023).
- [61] G. L. Stamokostas and G. A. Fiete, Mixing of $t_{2g} - e_g$ orbitals in $4d$ and $5d$ transition metal oxides, *Physical Review B* **97**, 085150 (02/26/ 2018).

ACKNOWLEDGMENTS

Work at Brookhaven and Harvard was supported by the U.S. Department of Energy, Office of Science, Office of Basic Energy Sciences, under Award Number DE-SC0012704. This research used resources of the Advanced Photon Source, a U.S. Department of Energy (DOE) Office of Science User Facility at Argonne National Laboratory and is based on research supported by the U.S. DOE Office of Science-Basic Energy Sciences, under Contract No. DE-AC02-06CH11357.

AUTHOR CONTRIBUTIONS

T.R., Y.S., & R.M.K. performed the calculations. Y.S., S.F.R.T., J.S., W.H., M.H.U., D.C., M.M., and

M.P.M.D. performed the measurements. P.B. prepared the crystals. The paper was written by T.R., Y.S., M.M., M.P.M.D. & R.M.K. with input from all co-authors.

ADDITIONAL INFORMATION

Correspondence and requests for materials should be addressed to T.R., Y.S., M.P.M.D, or R.M.K.

COMPETING FINANCIAL INTERESTS

The authors declare no competing interests.

Witnessing Quantum Entanglement Using Resonant Inelastic X-ray Scattering Supplementary Information

Tianhao Ren,^{1,*} Yao Shen,^{1,2,†} Sophia F. R. TenHuisen,³ Jennifer Sears,¹ Wei He,¹ Mary H. Upton,⁴
Diego Casa,⁴ Petra Becker,⁵ Matteo. Mitrano,³ Mark P. M. Dean,^{1,‡} and Robert M. Konik^{1,§}

¹Condensed Matter Physics and Materials Science Division,
Brookhaven National Laboratory, Upton, New York 11973, USA

²Beijing National Laboratory for Condensed Matter Physics,
Institute of Physics, Chinese Academy of Sciences, Beijing 100190, China

³Department of Physics, Harvard University, Cambridge, Massachusetts 02138, USA

⁴Advanced Photon Source, Argonne National Laboratory, Argonne, Illinois 60439, USA

⁵Section Crystallography, Institute of Geology and Mineralogy, University of Cologne, 50939 Köln, Germany

(Dated: April 10, 2024)

Supplementary Note 1: Transition Operators

In the formula for the RIXS intensity presented in the main text, we encounter the transition operators $\mathcal{D}_i(\mathbf{k}_i, \boldsymbol{\epsilon}_i)$, $\mathcal{D}_f(\mathbf{k}_o, \boldsymbol{\epsilon}_o)$. Under the dipole approximation, they can be written as [1]

$$\begin{aligned}\hat{\mathcal{D}}_i &= \sum_{a=x,y,z} \epsilon_{i,a} \hat{T}_{i,a}, & \hat{\mathcal{D}}_o^\dagger &= \sum_{a=x,y,z} \epsilon_{o,a}^* \hat{T}_{o,a}^\dagger, \\ \hat{T}_{i,x} &= e^{i\mathbf{k}_i \cdot \mathbf{R}} \hat{x}_R, & \hat{T}_{i,y} &= e^{i\mathbf{k}_i \cdot \mathbf{R}} \hat{y}_R, & \hat{T}_{i,z} &= e^{i\mathbf{k}_i \cdot \mathbf{R}} \hat{z}_R, \\ \hat{T}_{o,x} &= e^{i\mathbf{k}_o \cdot \mathbf{R}} \hat{x}_R, & \hat{T}_{o,y} &= e^{i\mathbf{k}_o \cdot \mathbf{R}} \hat{y}_R, & \hat{T}_{o,z} &= e^{i\mathbf{k}_o \cdot \mathbf{R}} \hat{z}_R,\end{aligned}\tag{1}$$

where \mathbf{R} is the coordinate for the scattering site- R , and $\hat{x}_R, \hat{y}_R, \hat{z}_R$ are position operators of electrons bound to the site- R .

Supplementary Note 2: Quantum Fisher Information

We consider a Hermitian operator \hat{A} . For a pure state, the QFI is expressible as [2]

$$F_Q(\rho, \hat{A}) = 4 \left(\langle \psi | \hat{A}^2 | \psi \rangle - \langle \psi | \hat{A} | \psi \rangle^2 \right).\tag{2}$$

If instead of a pure state, the quantum state is described by a thermal density matrix given by $\rho = \sum_k \lambda_k |k\rangle \langle k|$, where λ_k is the k -dependent Boltzmann factor, the QFI is expressible as [2]

$$F_Q(\rho, \hat{A}) = 2 \sum_{k,k'} \frac{(\lambda_k - \lambda_{k'})^2}{\lambda_k + \lambda_{k'}} |\langle k | \hat{A} | k' \rangle|^2.\tag{3}$$

Supplementary Note 3: Quantum Fisher Information and Susceptibility

To relate the QFI for a thermal ensemble to the dynamic susceptibility with a Hermitian operator \hat{A} [3], let's express the dynamic susceptibility χ''_{AA} in terms of the Lehmann representation:

$$\chi''_{AA}(\omega) = \frac{1}{Z} \sum_{m,n} e^{-\beta E_m} (1 - e^{-\beta \omega}) \left| \langle m | \hat{A} | n \rangle \right|^2 \delta(\omega + E_m - E_n).\tag{4}$$

Using the fact that

$$\int_{-\infty}^{\infty} d\omega \tanh\left(\frac{\beta\omega}{2}\right) \delta(\omega + E_m - E_n) = \tanh\left(\frac{\beta(E_n - E_m)}{2}\right) = \frac{\rho_m - \rho_n}{\rho_m + \rho_n},\tag{5}$$

* tren@bnl.gov

† yshen@iphy.ac.cn

‡ mdean@bnl.gov

§ rmk@bnl.gov

Supplementary Table I. Full list of parameters used in the exact diagonalization (ED) calculations for $\text{Ba}_3\text{TaIr}_2\text{O}_9$. As mentioned in the main text, the crystal field splitting parameters such as θ and κ are defined in Ref. 4, and ζ is the spin-orbit coupling parameter for the Ir 5d orbitals while the one for the 2p core orbitals is fixed to the atomic value 1140.332 eV. The inverse core-hole lifetime is set to the atomic value 2.47 eV. All parameters except θ and κ are in units of eV.

Crystal field splitting and spin-orbit coupling				Hopping integrals		
$10D_q$	θ	κ	ζ	$V_{dd\sigma}$	$V_{dd\pi}$	$V_{dd\delta}$
3.5	49.00	0.1	0.33	-0.96	-0.60	0.20
Core-hole potential				On-site Coulomb interactions		
F_{dp}^0	F_{dp}^2	G_{dp}^1	G_{dp}^3	F_{dd}^0	F_{dd}^2	F_{dd}^4
2.574	0.927	0.800	0.475	2.543	3.446	2.154

it can easily verify that

$$F_Q(\rho, \hat{A}) = 2 \int_{-\infty}^{\infty} d\omega \tanh\left(\frac{\beta\omega}{2}\right) \chi''_{AA}(\omega) = 4 \int_0^{\infty} d\omega \tanh\left(\frac{\beta\omega}{2}\right) \chi''_{AA}(\omega), \quad (6)$$

where the fact $\chi''_{AA}(\omega) = -\chi''_{AA}(-\omega)$ is used. We have generalized the above formulation to a non-Hermitian operator \hat{A} , in which case, the QFI is modified as

$$\begin{aligned} F_Q(\rho, \hat{A}_{\text{Re}}) + F_Q(\rho, \hat{A}_{\text{Im}}) &= 2 \int_{-\infty}^{\infty} d\omega \tanh\left(\frac{\beta\omega}{2}\right) [\chi''_{\hat{A}_{\text{Re}}\hat{A}_{\text{Re}}}(\omega) + \chi''_{\hat{A}_{\text{Im}}\hat{A}_{\text{Im}}}(\omega)] \\ &= \int_{-\infty}^{\infty} d\omega \tanh\left(\frac{\beta\omega}{2}\right) [\chi''_{\hat{A}\hat{A}^\dagger}(\omega) + \chi''_{\hat{A}^\dagger\hat{A}}(\omega)] \\ &= 2 \int_0^{\infty} d\omega \tanh\left(\frac{\beta\omega}{2}\right) [\chi''_{\hat{A}\hat{A}^\dagger}(\omega) + \chi''_{\hat{A}^\dagger\hat{A}}(\omega)], \end{aligned} \quad (7)$$

where we have used the fact that $\chi''_{\hat{A}\hat{A}^\dagger}(\omega) = -\chi''_{\hat{A}^\dagger\hat{A}}(-\omega)$. The efficiency of this combined QFI as an entanglement witness can be seen from the following inequality:

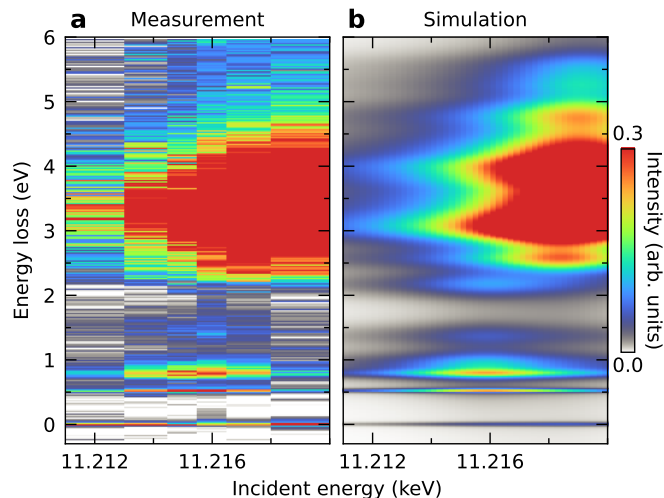
$$\min \left\{ \frac{F_Q(\rho, \hat{A}_{\text{Re}})}{\sum_{i=1}^N (\Delta a_{i,\text{Re}})^2}, \frac{F_Q(\rho, \hat{A}_{\text{Im}})}{\sum_{i=1}^N (\Delta a_{i,\text{Im}})^2} \right\} \leq \frac{F_Q(\rho, \hat{A}_{\text{Re}}) + F_Q(\rho, \hat{A}_{\text{Im}})}{\sum_{i=1}^N [(\Delta a_{i,\text{Re}})^2 + (\Delta a_{i,\text{Im}})^2]} \leq \max \left\{ \frac{F_Q(\rho, \hat{A}_{\text{Re}})}{\sum_{i=1}^N (\Delta a_{i,\text{Re}})^2}, \frac{F_Q(\rho, \hat{A}_{\text{Im}})}{\sum_{i=1}^N (\Delta a_{i,\text{Im}})^2} \right\}, \quad (8)$$

so it racks in between the entanglement witnesses provided by \hat{A}_{Re} and \hat{A}_{Im} individually.

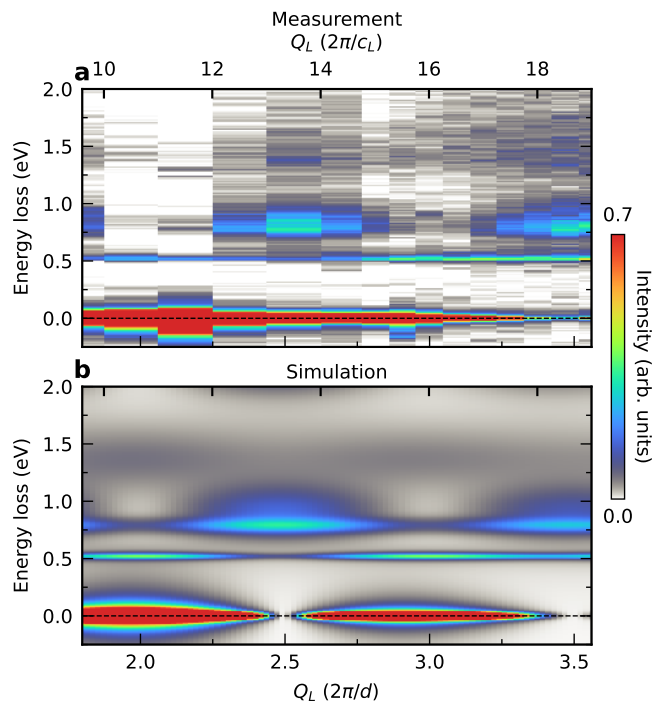
Supplementary Note 4: Detection of Quantum Entanglement in $\text{Ba}_3\text{TaIr}_2\text{O}_9$.

Apart from $\text{Ba}_3\text{CeIr}_2\text{O}_9$, we have also performed the analysis for the isostructural $\text{Ba}_3\text{TaIr}_2\text{O}_9$. In this material, 11 electrons are shared between these two Ir ions instead of 10 in $\text{Ba}_3\text{CeIr}_2\text{O}_9$, leading to distinct RIXS features. We follow the same strategy as the main text and use the codebase EDRIXS [1] with tuned parameters in Table I to reproduce the experimentally measured RIXS intensity, and construct the corresponding RIXS operator at the same time. To mimic the observed lineshape of the excitation peaks, the final-state energy loss spectra are broadened using multiple pseudo-Voigt profiles with the fraction fixed to 0.5 and full-widths at half-maximum of 0.044 and 0.108 eV for the first and second excitation peaks, respectively, and 0.3 eV for the rest of them. The comparisons between the measurement and simulation are shown in Figs. 1, 2, and 3, exhibiting excellent agreement. Using the constructed RIXS operator, the nQFI for $\text{Ba}_3\text{TaIr}_2\text{O}_9$ is subsequently calculated for different incident energies and momentum transfers, and the results are shown in Figs. 4 and 6. To explore the polarization as yet another witness selector, we simulate an experimental setup that can discriminate the final state polarization using the tuned parameters. The results are shown in Figs. 5 and 6. We can see that all these results are consistent with those for $\text{Ba}_3\text{CeIr}_2\text{O}_9$, which supports the idea that our approach can be applied to many real quantum materials with strong correlations.

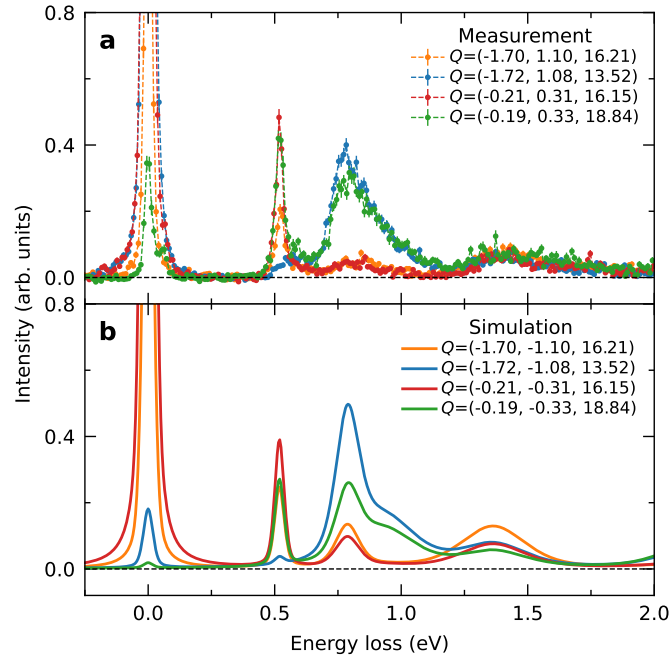
-
- [1] Y.L. Wang, G. Fabbris, M.P.M. Dean, and G. Kotliar, “Edrixs: An open source toolkit for simulating spectra of resonant inelastic x-ray scattering,” *Computer Physics Communications* **243**, 151–165 (2019).
[2] Luca Pezzé and Augusto Smerzi, “Quantum theory of phase estimation,” *arXiv 1411.5164* (2014).



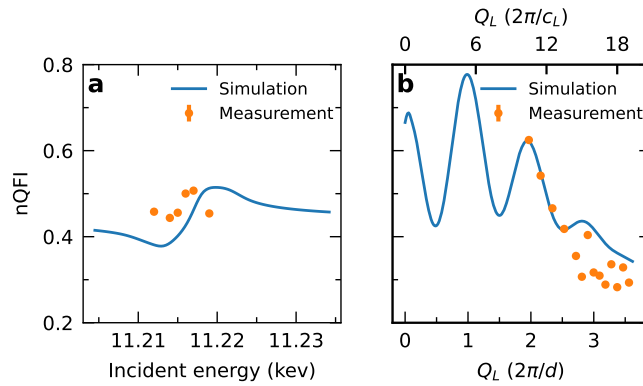
Supplementary Figure 1. Comparison of the incident energy dependence of the RIXS spectra between measurement and simulation. **a**, Measured RIXS spectra with varying incident energy at fixed momentum transfer with $L = 18.4$ in reciprocal lattice units (r.l.u.). The signals below 1.5 eV energy loss correspond to intra- t_{2g} transitions while the ones above 1.5 eV mainly come from inter- t_{2g} - e_g transitions. **b**, Calculated incident-energy-dependent RIXS spectra at the same fixed momentum transfer.



Supplementary Figure 2. Comparison of the L dependence of the RIXS spectra between measurement and simulation. **a**, Measured L -dependent RIXS spectra showing periodic modulation, and the incident energy $\hbar\omega_{\text{in}}$ is fixed to 11.216 keV. Only the intra- t_{2g} transitions are presented since they are the dominating signals at this particular incident energy. **b**, Calculated L -dependent RIXS spectra at the same fixed incident energy. Q_L is the momentum transfer along the L direction. For convenience, the same momentum scale is displayed in two units. On top, we use units of $2\pi/c_L$ where c_L is the unit cell lattice constant along L direction. On bottom, we use units of $2\pi/d$, where d is the distance between the two dimers along the L direction.

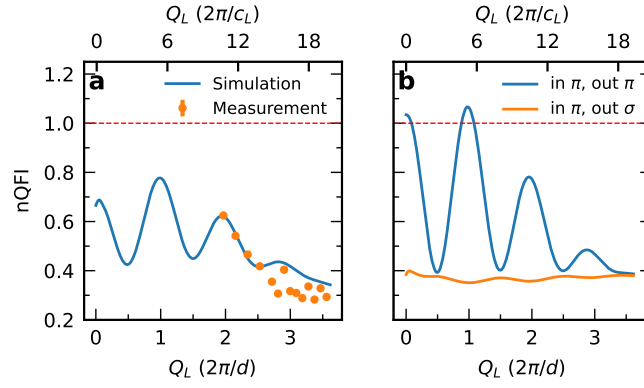


Supplementary Figure 3. Comparison of RIXS spectra between measurement and simulation at representative momentum transfers. **a**, Representative RIXS spectra at the indicated momentum transfers in r.l.u., and the incident energy $\hbar\omega_{\text{in}}$ is fixed to 11.216 keV. Only the intra- t_{2g} transitions are presented since they are the dominating signals at this particular incident energy. **b**, Calculated RIXS spectra at the same momentum transfers and the same fixed incident energy.

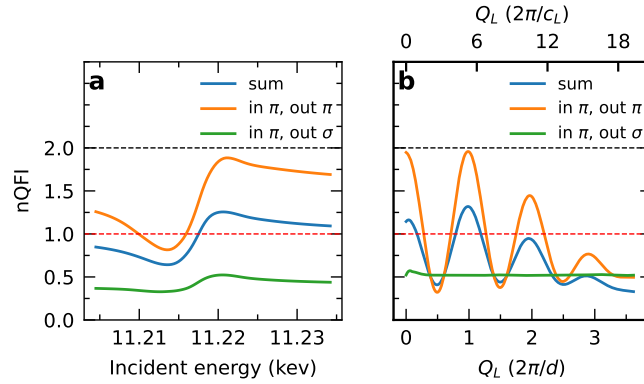


Supplementary Figure 4. The entanglement witness - comparison between simulation and measurement. **a** is for fixed momentum transfer with $L = 18.4$ r.l.u and different incident energies **b** is for fixed incident energy at $\hbar\omega_{\text{in}} = 11.216$ keV and different momentum transfers.

- [3] Philipp Hauke, Markus Heyl, Luca Tagliacozzo, and Peter Zoller, “Measuring multipartite entanglement through dynamic susceptibilities,” *Nature Physics* **12**, 778–782 (2016).
 [4] K. I. Kugel, D. I. Khomskii, A. O. Sboychakov, and S. V. Streltsov, “Spin-orbital interaction for face-sharing octahedra: Realization of a highly symmetric SU(4) model,” *Phys. Rev. B* **91**, 155125 (2015).



Supplementary Figure 5. Witness measurements with scattered x-ray polarization discrimination can detect entanglement. **a** reproduces the right panel of Fig. 4; **b** is for the same setup as **a** but with final state polarization discrimination. The red dashed line is the nQFI threshold for 2-partite entanglement. The legend in the right panel documents the polarizations for the final state (out) and incident beam (in), where the π polarization is in the incident plane, σ polarization is out of the incident plane.



Supplementary Figure 6. Using higher incident energies allows entanglement detection. **a** is for fixed momentum transfer with $L = 6$ r.l.u.; **b** is for fixed incident energy at $\hbar\omega_{\text{in}} = 11.220$ keV and different momentum transfers. Both summation (blue) and discrimination of the scattered x-ray polarizations (orange and green) are shown. The red dashed line is the nQFI threshold for 2-partite entanglement, and the black dashed line is the upper bound for nQFI in a dimer system.